

Microstructure and crystallographic texture of an ultrafine grained C–Mn steel and their evolution during warm deformation and annealing

R. Song¹, D. Ponge, D. Raabe^{*}, R. Kaspar

Max-Planck-Institut für Eisenforschung, Max-Planck-Strasse 1, 40237 Düsseldorf, Germany

Received 26 August 2004; received in revised form 19 October 2004; accepted 22 October 2004

Available online 8 December 2004

Abstract

The evolution of microstructure and texture of a 0.2%C–Mn steel during large strain warm deformation and subsequent annealing has been investigated. The process of grain subdivision during warm deformation is essential for the formation of ultrafine grains in such a material. The study reveals that pronounced recovery instead of primary recrystallization is required to obtain a large fraction of high-angle grain boundaries (HAGBs) as a prerequisite for the development of ultrafine grains in the course of warm deformation. The prevalence of primary recrystallization instead of recovery is not generally beneficial in this context since it reduces significantly the dislocation density and removes the substructure which is important for the gradual formation of subgrains and, finally, of ultrafine grains which are surrounded by HAGBs. Consistently, the texture of the ultrafine grained 0.2%C–Mn steel observed after large strain warm deformation and subsequent annealing, consists primarily of the α -((1 1 0)||RD) texture fiber which indicates strong recovery. The γ -((1 1 1)||ND) texture fiber which is typical of recrystallized rolled ferritic steels does not appear. The process occurring during the deformation and subsequent annealing can, therefore, be interpreted as a pronounced recovery process during which new grains are created without preceding nucleation.

© 2004 Acta Materialia Inc. Published by Elsevier Ltd. All rights reserved.

Keywords: Steel; Texture; EBSD; Recrystallization; Recovery; Ultrafine grains

1. Introduction

1.1. Importance of ultrafine grains for steels

Among the different strengthening mechanisms, grain refinement is the only method to improve both strength and toughness simultaneously. Therefore, ultrafine grained steels with relatively simple chemical compositions, strengthened primarily by grain refinement, have great potential for replacing alloyed high strength steels.

The main benefits behind such a strategy are to avoid additional alloying elements, to skip complicated additional heat treatments like soft annealing, quenching and tempering, and to improve weldability owing to the reduced required content of carbon and other alloying elements when compared with high strength quenched and tempered steels. A further high potential area of ultrafine grained steels is the domain of high strain rate superplasticity at medium and elevated temperatures.

In general, the term *ultrafine grain* is used for average grain sizes between 1 and 2 μm in diameter; the term *submicron structure* refers to grain sizes between 100 and 1000 nm; and the term *nano-structure* means grain sizes below 100 nm.

^{*} Corresponding author. Tel.: +49 211 6792 278; fax: +49 211 6792 333.

E-mail addresses: song@mpie.de (R. Song), raabe@mpie.de (D. Raabe).

¹ Tel.: +49 211 6792 471; fax: +49 211 6792 333.

1.2. Methods of producing ultrafine grained steels

In recent years it has become a worldwide issue to develop manufacturing processes for obtaining ultrafine grained steels. Currently, there are two main groups of laboratory methods for refining ferrite grains down to the ultrafine grain regime in bulk steels. The first group comprises the various severe plastic deformation (SPD) techniques. The second group comprises advanced thermomechanical processes.

The SPD techniques aim at producing ultrafine grained steels with average grain diameters in the sub-micron regime by using very large plastic strains. The main SPD techniques are equal channel angular pressing (ECAP) [1,2], accumulative roll bonding (ARB) [3,4], and bi-directional deformation [5]. The accumulated plastic strains required to obtain submicron-sized grains by SPD are of the order of 4 using ECAP and of the order of 5–6 using the ARB process, respectively (true logarithmic strains). For the SPD methods a well designed strain path is more important and also more feasible than a precisely controlled temperature path.

The advanced thermomechanical processes, in contrast, pursue alternative microstructure strategies to produce ultrafine ferrite grains, for instance, by exploiting strain-induced ferrite transformation (i.e. transformation during rather than after deformation) [6], dynamic recrystallization of the austenite during hot deformation with subsequent $\gamma \rightarrow \alpha$ (austenite to ferrite) transformation [7], hot rolling in the intercritical region (i.e. in the austenite + ferrite two-phase region) [8], and/or dynamic recrystallization of the ferrite during warm rolling [9]. Table 1 gives a summary of the various process techniques, the ferrite grain sizes obtained for various types of steels, and the associated microstructural mechanisms which were suggested by the respective authors.

Compared with the SPD methods, the advanced thermomechanical processing routes require a relatively low accumulated logarithmic strain of about 2.2–3.6 to produce ultrafine grained steels (except for the strain-induced ferrite transformation technique which typically requires lower strain). A further important difference between the two approaches is that the advanced thermomechanical processing methods are less effective with respect to grain refinement, but they are more efficient with respect to large sample sizes when compared with the SPD methods. An important issue in that context, however, is that in the case of large sample sizes the strain and cooling paths have to be carefully controlled since they are key parameters to govern the final grain size within relatively small process windows.

A further difference between these two groups of methods is that the advanced thermomechanical methods are continuous processes and can only work when they exploit phase transformation. The SPD methods, on the other hand, are preferred for relatively soft materials owing to the huge accumulated strains required (the logarithmic strains are always larger than 4) when aiming at producing samples with ultrafine microstructures.

1.3. Scope of this study

In this study, we introduce a new concept for producing ultrafine grained C–Mn steels by thermomechanical processing. In particular, a considerable effort was made to understand the details of the evolution of microstructure and crystallographic texture during the large strain warm deformation and subsequent annealing treatment by using field-emission scanning electron microscopy (FE-SEM) and high resolution electron backscatter diffraction (EBSD). The influence of the fine cementite particles on the formation of ultrafine microstructures and

Table 1
Overview of the different techniques which are used to produce ultrafine grains in steels

Techniques	Ferrite grain size achieved	Log strain imposed [1]	Deformation temperature [K]	Steels/composition [wt%]	References
ECAP	0.3 μm	4	623	0.15C–1.1Mn–0.25Si	[10]
ARB	0.4 μm	5.6	773	IF steel	[11]
Multiple compression	0.3 μm	6.4	873	Austenitic stainless steel	[12]
Strain-induced ferrite transformation	1.0 μm (strip surface)	0.36	1053	0.06C–0.59Mn	[6]
DRX ^a during hot deformation	2–5 μm	Final rolling 2.2–3.6	1153–1033	0.11C–1.45Mn– 0.34Si–0.068Nb	[7]
Deformation in the intercritical region	2.1 μm	2.3	973	0.17C–1.32Mn– 0.44Si–0.15Nb	[13]
Warm rolling in the ferrite region	1–3 μm	Final rolling ~0.55 \times 5	below A_{r1} ^b	IF steel	[9]

The abbreviations are: ECAP: equal channel angular pressing; ARB: accumulative roll bonding.

^a Dynamic recrystallization.

^b Austenite to pearlite transformation temperature during cooling.

in particular on the recovery process were studied by use of transmission electron microscopy (TEM).

By studying the key mechanisms associated with the formation of ultrafine grained microstructures in the course of the thermomechanical routes investigated in this work we hope to develop well tailored and microstructurally guided approaches to the large scale production of ultrafine grained steels.

2. Experimental methods

2.1. Specimen preparation and experimental set-up

Table 2 shows the chemical composition of the plain C–Mn steel used in this work. The calculated A_{e3} temperature (equilibrium austenite to ferrite transformation temperature) amounts to 1093 K [14]. The laboratory samples were machined directly from the cast ingot into rectangular parallelepiped samples of $50 \times 40 \times 60 \text{ mm}^3$ (width \times length \times height). The plane strain compression tests were conducted by using a large scale 2.5 MN hot press at the Max-Planck-Institut für Eisenforschung [15].

2.2. Outline of the experimental routes

All specimens were pre-processed by an identical austenitization and cooling route in order to provide a homogeneous ferrite-pearlite microstructure before the application of the different actual thermomechanical techniques. This procedure was conducted as follows: Since the refinement of austenite is essential for obtaining small grains after transformation the experiments were carried out at a low austenitization temperature. After reheating with a heating rate of 10 K/s, the samples were austenitized at 1193 K (100 K above A_{e3}) for 3 min to achieve a fine austenite grain size. After air cooling to 1143 K, a one-step deformation pass was exerted imposing a logarithmic strain of $\varepsilon = 0.3$ at a strain rate of 10 s^{-1} in order to obtain fully recrystallized austenite. This was followed by a controlled cooling procedure down to the pearlite finish temperature of 823 K at a cooling rate of 6.5 K/s which is the maximum cooling rate to obtain a bainite free ferrite-pearlite microstructure. After this primary treatment which was identical for all specimens, the following different experimental routes were carried out to provide sets of different sample states:

(a) *Conventional route*: In order to study the initial ferrite-pearlite microstructure before large strain warm deformation, a conventional thermomechanical route was applied. This means that after the controlled cooling

and 2 min holding period at 823 K as described above, the samples were water quenched in order to obtain a bainite-free ferrite-pearlite microstructure, Fig. 1(a).

(b) *Ultrafine grain route*: After a 2 min holding period at 823 K, the large strain warm deformation was performed by applying a four-pass plane strain compression process with an inter-pass time of 0.5 s. Each of the four subsequent steps imposed a logarithmic strain of $\varepsilon = 0.4$ accumulating to a total strain of $\varepsilon = 1.6$. Each pass was conducted at a strain rate of 10 s^{-1} . Subsequently, an annealing treatment of 2 h at 823 K was exerted, Fig. 1(b).

(c) *Route for studying microstructure evolution during warm deformation*: In order to study the details of the evolution of the ultrafine grained microstructure and of the crystallographic texture in the course of the large strain warm deformation procedure, samples were water quenched after intermediate true accumulated strains of $\varepsilon = 0.4, 0.8, 1.2$, and 1.6 , respectively, Fig. 1(c).

(d) *High temperature annealing route*: After conducting the large strain warm deformation at 823 K as outlined above the steel was annealed for 2 h at an elevated temperature of 973 K, in order to study the effect of the cementite particles on grain growth at high temperatures above the recrystallization temperature, Fig. 1(d).

2.3. Characterization of microstructure and crystallographic texture

2.3.1. Light optical microscopy

The specimens for light optical microscopy were mechanically polished to a $1 \mu\text{m}$ finish and etched using a 1% Nital solution. Micrographs were taken at those locations within the samples where the local strain was equal to the nominal strain according to finite element calculations.

2.3.2. Scanning electron microscopy

In this study a JSM-6500F field-emission SEM was used. The JSM-6500F offers high lateral resolution and a large probe current density at small probe diameters which is an essential condition for conducting large-scale high-resolution EBSD (see ensuing section). Sample preparation for microstructural analysis in the SEM was the same as that for the optical metallography.

2.3.3. Microtexture analysis by electron backscatter diffraction

The EBSD measurements were carried out at an accelerating voltage of 15 kV and an emission current of about $100 \mu\text{A}$ at a specimen inclination angle of 70° towards the camera. Orientation maps were taken from

Table 2
Chemical composition of plain C–Mn steel

Elements	Fe	C	Si	Mn	P	S	Al	N
Mass %	Bal.	0.22	0.21	0.74	0.004	0.003	0.029	0.001

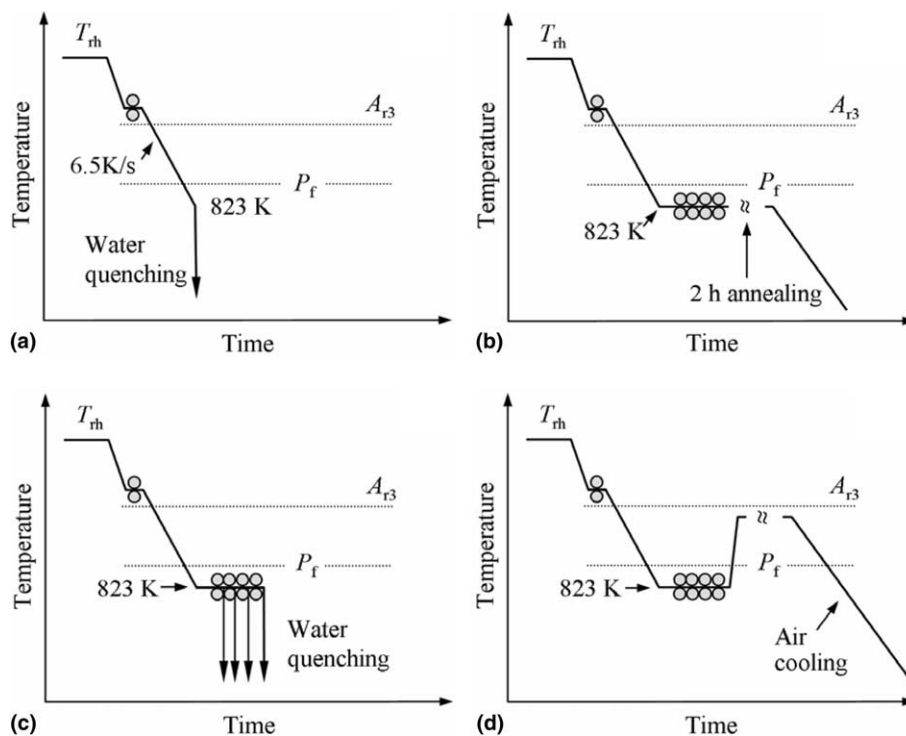


Fig. 1. Processing schedules for the plane strain warm compression tests: (a) conventional route for producing coarse microstructures; (b) ultrafine grain route; (c) processing route for the investigation of details of the microstructure evolution during warm deformation ($\epsilon = 0.4, 0.8, 1.2, 1.6$); and (d) high temperature annealing route after large strain warm deformation. (T_{rh} , reheating temperature; A_{r3} , austenite to ferrite transformation temperature; P_f , pearlite finish temperature.)

50 $\mu\text{m} \times 50 \mu\text{m}$ areas on longitudinal sample sections at a step size of 100 nm in both directions. The microtexture data were used to analyze the local lattice orientation, the grain boundary topology, and the grain boundary character distribution in the samples. The latter aspect is of particular relevance in the context of this study since the optimization of ultrafine grained microstructures aims at a large density of high-angle grain boundaries (HAGBs) which can only be verified by the use of a high resolution EBSD technique in such microstructures, as opposed to conventional metallographic characterization. HAGBs are homophase interfaces with a misorientation angle of $\theta \geq 15^\circ$. Lower values of the local misorientation ($2^\circ \leq \theta < 15^\circ$) represent low-angle grain boundaries (LAGBs).

2.3.4. Characterization of grain size

Ultrafine grains produced by large strain deformation in steels are often not completely surrounded by HAGBs, but some of the grain boundary segments may have low-angle misorientation character. Compared with LAGBs, HAGBs are more important for strengthening. Also, HAGBs are more efficient in improving the toughness of steels. The reason is that if an intragranular cleavage crack moves across a HAGBs, the crack front usually branches according to the change of the preferred fracture plane. Such branching results in

additional fracture work. In contrast, when a crack meets a low-angle grain boundary, the crack can typically penetrate such an interface without a substantial change in the propagation direction and without branching. Therefore, it is necessary to clearly identify and quantitatively characterize the grain boundary character together with the analysis of the grain size [16]. Also, the careful characterization of the average grain size is essential for predicting the mechanical properties of steels based on the Hall–Petch relationship. For this reason, in this study the ferrite grain size (counting only grains with a grain boundary misorientation $\theta \geq 15^\circ$) produced by the ultrafine grain route (Fig. 1(b)) was measured by use of EBSD maps in conjunction with the mean linear intercept method. The spacing between the grain boundaries was measured both, along the normal direction (ND) and the rolling direction (RD). The grain size is then defined as the average diameter of the equivalent area circles which match the area of the elliptically shaped grains. The grain shape aspect ratio of each grain was defined as the grain length measured in the rolling direction divided by that measured in the normal direction.

2.3.5. Transmission electron microscopy

The TEM observations were carried out using a Philips CM20 instrument. The size distribution of the

cementite particles was determined and characterized in terms of the mean linear intercepts from the SEM and bright field TEM images. The TEM samples were produced by mechanical polishing to a thickness of about 50 μm , followed by electropolishing using a Tenupol double jet instrument in 95% $\text{C}_2\text{H}_4\text{O}_2$ + 5% HClO_4 at 288 K and 40 V.

3. Experimental results

3.1. Evolution of microstructure and crystallographic texture during warm deformation

Figs. 2–4 document the microstructure evolution of the steel during deformation and subsequent annealing. Fig. 2(a) shows the initial ferrite-pearlite microstructure before the warm deformation. Figs. 2(b) and 4(a) show that the ferrite-pearlite microstructures were finer after the first deformation step ($\varepsilon = 0.4$) than before the warm deformation. Also, the grain shape is elongated in the rolling direction. Although the ferrite grain boundaries are clearly visible in Fig. 2(b) after the first warm deformation step of $\varepsilon = 0.4$ many details of a faint substructure appear as fine lines inside some of the ferrite grains.

After the second deformation step ($\varepsilon = 0.8$) the microstructure is too fine to be resolved by optical microscopy, Fig. 2(c). Using a higher magnification (see SEM image, Fig. 3(b)) reveals that the microstructure consists of ferrite and partially spheroidized cementite. The former pearlite colonies are elongated and can still be clearly distinguished. The fraction of HAGBs decreases, Fig. 4(b).

After the third deformation step ($\varepsilon = 1.2$) the average ferrite grain size decreases slightly and the grain shape aspect ratio remains practically unchanged, Fig. 4(a). On the other hand, the fraction of HAGBs has increased, Fig. 4(b). The details of the distributions of the grain boundary misorientations are shown in Fig. 5(b). The data reveal that the number fraction of grain boundary misorientations below 8° clearly decreases when compared with that after two deformation steps, Fig. 5(a). The texture at that stage is dominated by a pronounced α -($\langle 1\ 1\ 0 \rangle \parallel \text{RD}$) fiber, Fig. 6.

Most of the pearlite lamellae were spheroidized into cementite particles after four deformation steps ($\varepsilon = 1.6$), Fig. 3(c). The clear alignments of the cementite particles which decorate the ferrite grain boundaries still can be seen (arrow “1”). Different sizes of cementite particles (arrows “1” and “2”) and cementite fragments (arrow “3”) were inhomogeneously distributed within the ferrite matrix. The ferrite grain size decreases and the grain shape becomes more equiaxed with increasing strain, Fig. 4(a). The fraction of HAGBs remains practically unchanged, Fig. 4(b). The average misorientation angle increases to 27.2° , Fig. 5(c). Fig. 6 reveals that the fraction of the γ -($\langle 1\ 1\ 1 \rangle \parallel \text{ND}$)-texture-fiber increases relative to the α -texture fiber.

3.2. Microstructure and crystallographic texture after annealing

After annealing the samples (processed by four deformation steps $\varepsilon = 1.6$) for 2 h, there is nearly no change in the grain size. However, the grain shape becomes more equiaxed after that heat treatment, Fig. 4(a). Nearly

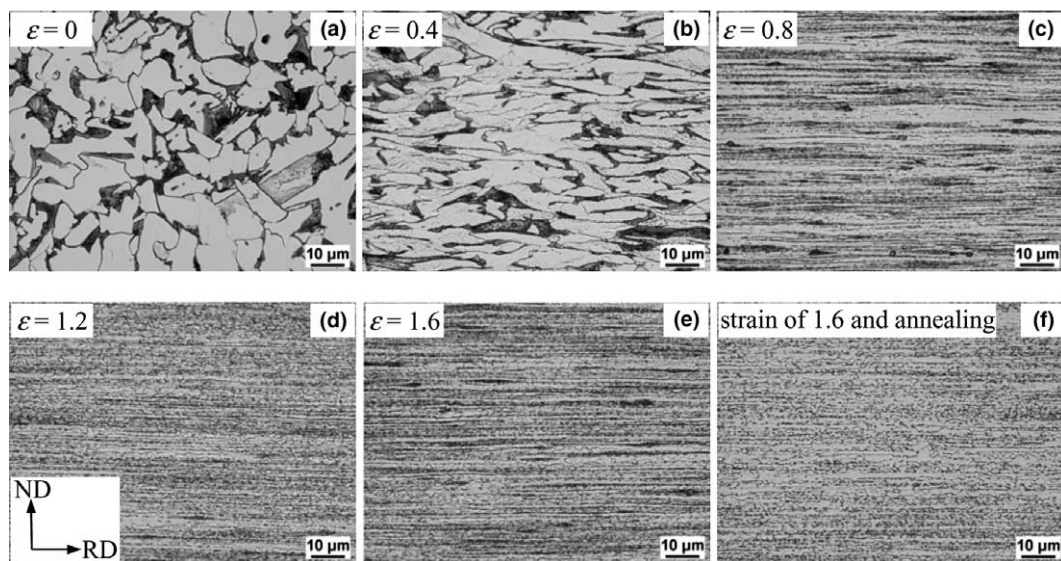


Fig. 2. Optical microstructures of the steel during warm deformation and subsequent annealing at 823 K, Fig. 1(b) and (c): (a) initial microstructure before large strain warm deformation; (b)–(e) microstructures after one to four deformation steps ($\varepsilon = 0.4$, 0.8, 1.2 and 1.6), respectively; (f) microstructure after four deformation steps and a subsequent 2 h annealing treatment at 823 K.

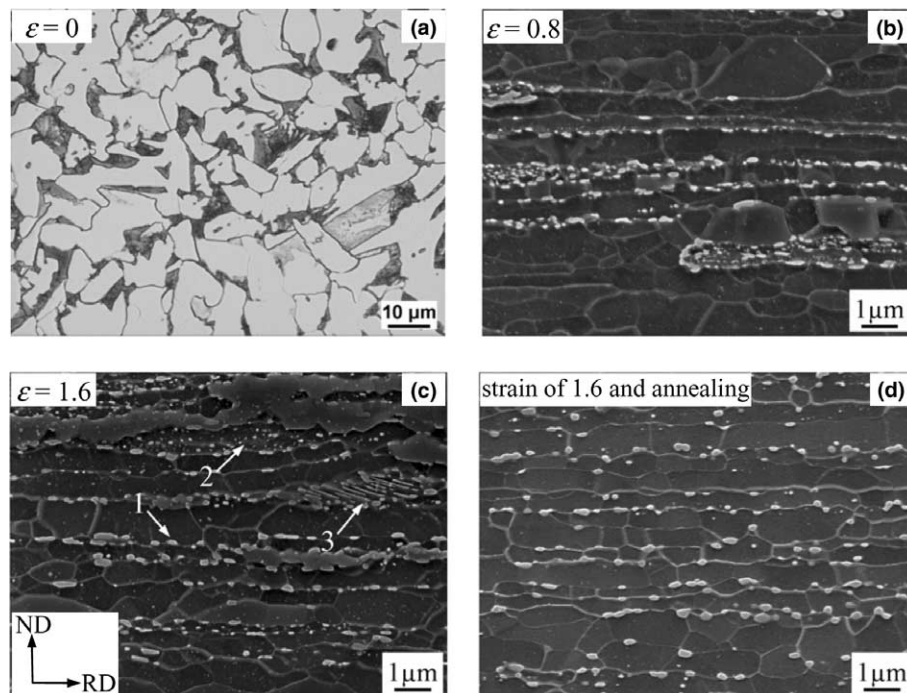


Fig. 3. Microstructural evolution of the steel during warm deformation and subsequent annealing at 823 K, Fig. 1(b) and (c): (a) initial microstructure before large strain warm deformation; (b,c) microstructures after two and four deformation steps ($\varepsilon = 0.8, 1.6$), respectively (arrow “1” points at a large cementite particle at a ferrite grain boundary; arrow “2” points at small cementite particles in the initial pearlite colony region; and arrow “3” points at a cementite lamella in the initial pearlite colony region); (d) microstructure after four deformation steps and a subsequent 2 h annealing treatment at 823 K.

all cementite fragments are spheroidized into globular particles and homogeneously distributed in the ferrite matrix, Fig. 3(d). The fraction of HAGBs hardly changes during annealing, Figs. 4(b) and 5(d). The crystallographic texture observed after the heat treatment is characterized by a strong α -fiber. This marks a strong difference to interstitial free steels, which typically show a pronounced γ -fiber texture after cold deformation and subsequent annealing [17–26], Fig. 6.

Fig. 7(a) shows the spatial distribution of the α - and γ -fiber texture components on longitudinal sections after warm deformation and subsequent annealing. The blue color indicates the α -fiber. The red color indicates the γ -fiber. The gradient in the color represents the angular deviation from a perfectly aligned α - or γ -fiber-texture, respectively. For instance, for the α -fiber a change in intensity of the blue color indicates a shift of the orientation from the exact fiber axis to a maximum deviation of 15° . The black lines indicate misorientations $\theta \geq 15^\circ$ between adjacent grains. The white lines indicate misorientations between 2° and 15° . Fig. 7(a) shows that the area fraction which is occupied by α -fiber orientations (blue color) decreases when the logarithmic strain increases from 1.2 to 1.6. However, after the annealing (Fig. 7(a)) the α -fiber orientations increase again substantially. The same tendency is documented in Fig. 6, i.e. the α -fiber first decreases when the strain increases

from 1.2 to 1.6 and then strongly increases after the annealing treatment. Fig. 7(b) documents the texture evolution in terms of the $\varphi_2 = 45^\circ$ sections through the orientation distribution function (ODF) during warm deformation and subsequent annealing.

3.3. Evolution of pearlitic cementite lamellae during warm deformation

During warm deformation the increase in strain leads to an alignment of the pearlitic cementite lamellae and, at a later stage, to an alignment of cementite strings. This entails anisotropic growth of the ferrite grains. Fig. 8 summarizes the effect of deformation on the microstructural evolution during warm deformation both, in terms of a schematic drawing and in terms of corresponding SEM micrographs. Fig. 8(a) shows the initial ferrite-pearlite microstructure. After some deformation, the pro-eutectoid ferrite grains and the pearlitic regions become elongated. The pearlitic cementite lamellae rotate perpendicular to the compression direction. At the same strain level, some pearlitic cementite lamellae disintegrate into short fragments, which decorate the grain boundaries of the pearlitic ferrite (Fig. 8(b)). After large strain deformation, these fragments spheroidize into discrete cementite particles. Smaller cementite particles are also observed inside the ferrite grains. Larger

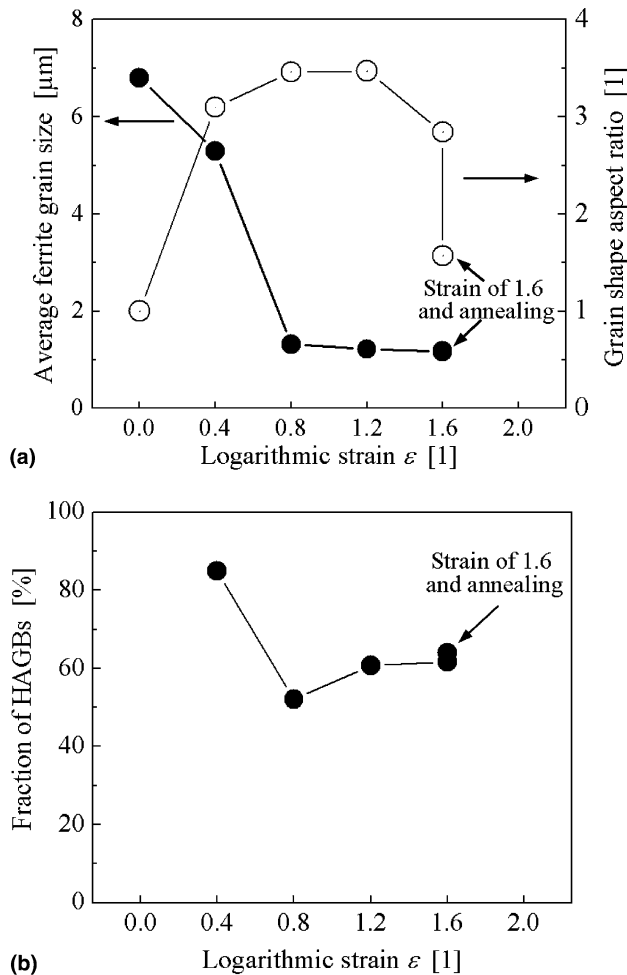


Fig. 4. Evolution of some important features of the grain characteristics of the steel during warm deformation and subsequent annealing at 823 K (Fig. 1(b)) (each deformation step imposed a true strain of $\epsilon = 0.4$ at a strain rate of $\dot{\epsilon} = 10 \text{ s}^{-1}$ (Fig. 1(c))); (a) average ferrite grain size and grain shape aspect ratio; (b) fraction of high-angle grain boundaries (HAGBs).

cementite particles are distributed at the ferrite grain boundaries and act as obstacles to grain boundary migration. After the large strain deformation the cementite particles are aligned in rows perpendicular to the compression direction. This impedes grain boundary migration in the compression direction, entailing an elongated grain shape. Most of the large flat pro-eutectoid ferrite grains are divided into several subgrains (Fig. 8(c)).

3.4. TEM analysis

The TEM micrographs of the steel after large strain warm deformation and direct water cooling are shown in Fig. 9(a), and after large strain warm deformation followed by a subsequent annealing in Fig. 9(b). All microstructures are characterized by ultrafine ferrite grains and globular cementite. The ferrite grain size hardly

changed during the post-deformation heat treatment (Fig. 9(b)), if compared to that observed directly after large strain warm deformation (Fig. 9(a)). A slight coarsening of the cementite particles occurs after the annealing. Two different size groups of cementite particles can be observed in the microstructure (Fig. 9(b)). The finer cementite particles (5–90 nm) are distributed inside the ferrite grains (see arrows 1). The planar arrays of larger cementite particles (90–350 nm) are located at the ferrite grain boundaries (see arrows 2), acting as obstacles impeding their migration. Fig. 9(c) and (d) shows the dislocation structures in the steel after large strain warm deformation and annealing, respectively. Dislocations were found in both, deformed and annealed samples.

In Fig. 10(a), the mutual crystallographic misorientations of local areas (adjacent grains or subgrains numbered by 1–6) were determined by means of Kikuchi analysis in the TEM using the method of Zaefferer [27,28]. The curvature of the subgrain boundary (misorientation 7.5°) demonstrates a pinning process of a particle on the ferrite grain boundary. Fig. 10(b) shows the dislocation structures and the individual cementite particles inside the ferrite matrix. The black arrows point at cementite particles as they pin dislocations (Fig. 10(b)).

3.5. High temperature annealing

Fig. 11 shows the image quality map, obtained from the EBSD measurements, of the steel after large strain warm deformation ($\epsilon = 1.6$) at 823 K and a subsequent 2 h heat treatment at 973 K. The map shows the same microstructure components as in the case of an annealing temperature of 823 K, namely, ferrite and globular cementite. Nevertheless, compared with the SEM micrograph of the steel presented in Fig. 3(d), also some coarse ferrite grains appear in the microstructure. A large number of cementite particles can be observed inside the coarser grains.

4. Discussion

4.1. Microstructure evolution of the ferrite during large strain warm deformation

Fig. 2 shows the effect of strain on the evolution of the microstructure during multi-step warm deformation. After the first moderate deformation step ($\epsilon = 0.4$) the average ferrite grain size and the aspect ratio increases along the rolling direction (Fig. 2(a) and (b)). The pro-eutectoid ferrite grain boundaries are visible. Some of the ferrite grains reveal an internal substructure which indicates the onset of strain-induced fragmentation in those crystallites [29]. After an increase of the

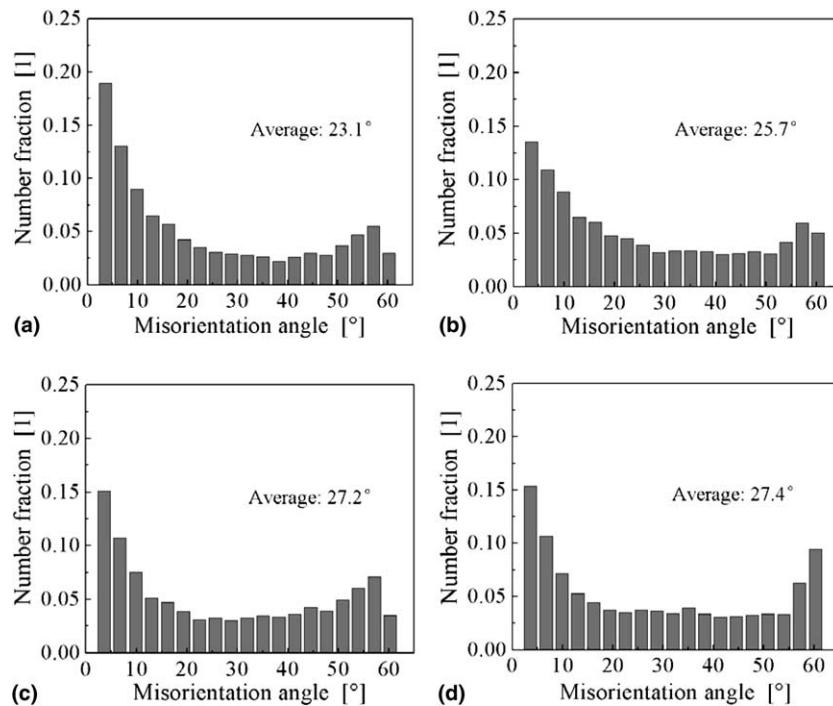


Fig. 5. Grain boundary misorientation distribution for the steel during warm deformation and subsequent annealing at 823 K, Fig. 1(b) and (c): (a)–(c) misorientation distribution after two to four deformation steps ($\varepsilon = 0.8, 1.2$ and 1.6), respectively; (d) misorientation distribution after four deformation steps and a subsequent 2 h annealing treatment at 823 K.

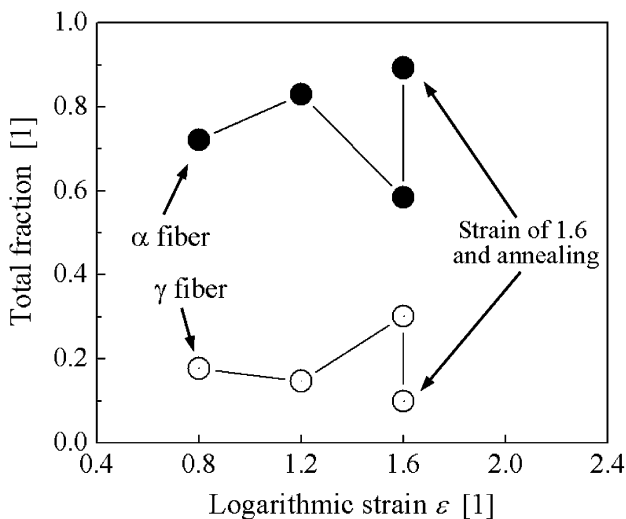


Fig. 6. Total fraction of α -(110) fiber and γ -(111) fiber for the steel during warm deformation (Fig. 1(c)) and subsequent annealing at 823 K (Fig. 1(b)), each deformation step with $\varepsilon = 0.4$ and $\dot{\varepsilon} = 10 \text{ s}^{-1}$.

accumulated logarithmic strain to 0.8 the ferrite grain size decreases rapidly and the grain shape becomes more elongated (Figs. 2(c) and 4(a)). The drop in the fraction of HAGBs (Fig. 4(b)) suggests that grain subdivision proceeds during deformation. The pearlite colonies are stretched along the rolling direction (Fig. 3(b)). A further increase in the accumulated true strain up to 1.6 en-

tails a relatively weak refinement of the ferrite grains (Fig. 4(a)).

These observations suggest a critical strain of about 0.8 for refining the microstructure. Such a threshold value was also reported by Shin and Prangnell [10,29,30] for a low carbon steel and for an Al–Mg alloy which were both processed by SPD. As reported by Tsuji [31] in-grain subdivision is of great importance for grain refinement especially when starting from an initially coarse microstructure. Both, the appearance of a more equiaxed grain structure after the large strain deformation and the notable increase in the fraction of HAGBs after this threshold strain (Figs. 4, 5(b) and (c)) can be attributed to pronounced recovery, especially to polygonization. Since this process leads in the end to a high fraction of HAGBs (but without the preceding motion of HAGBs) it can also be referred to as continuous recrystallization or, equivalently, as recrystallization in situ [32,33].

This interpretation is supported by two facts. First, the ferrite grain structures observed are elongated, i.e. the grain shape aspect ratio was about 2.8 after a true strain of $\varepsilon = 1.6$, Fig. 4(a). Second, numerous dislocations can be identified inside the grains, Fig. 9(c).

Recovery facilitates the deformation-induced gradual transition of LAGBs into HAGBs. Possible mechanisms in that context are the accumulation of geometrically necessary dislocations in the subgrain boundaries [34], the increase in the grain boundary misorientation which

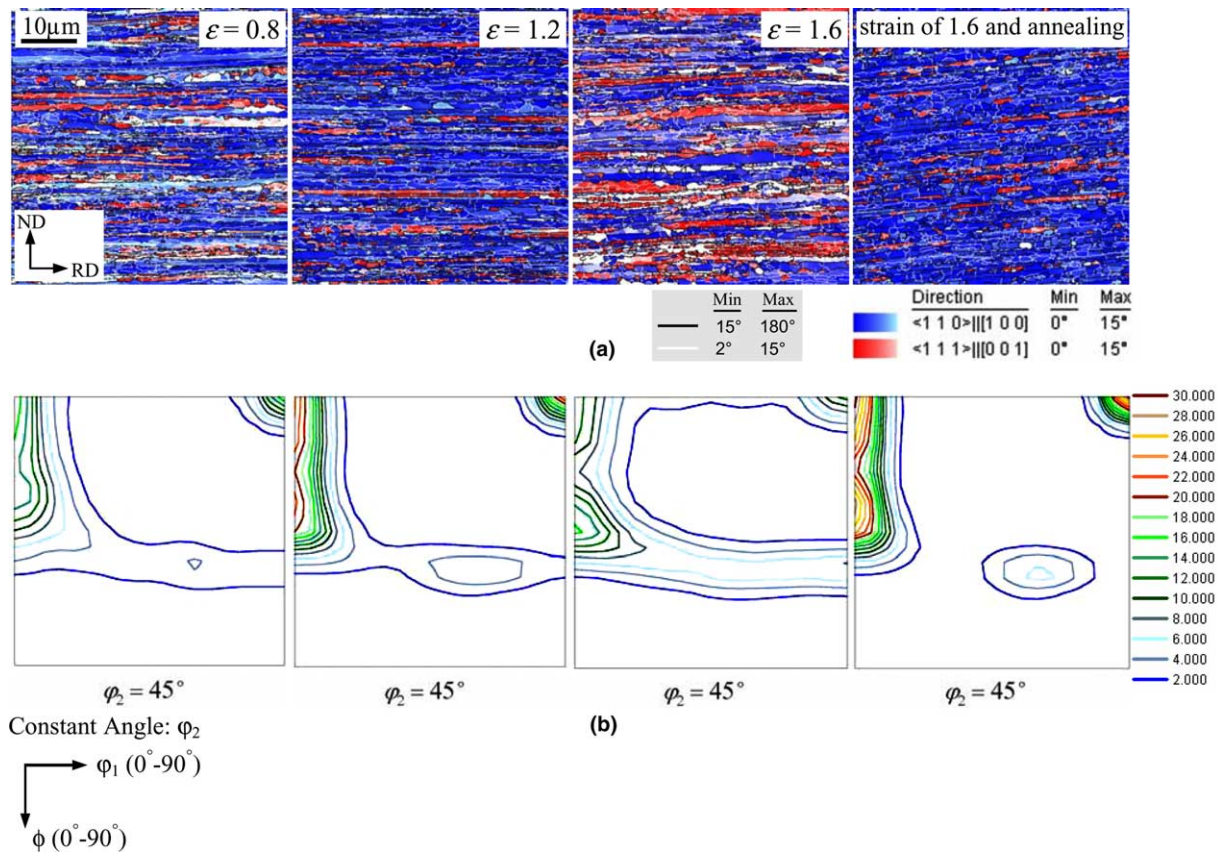


Fig. 7. Evolution of the crystallographic texture for the steel during warm deformation and subsequent annealing at 823 K (each deformation step imposed a true strain step of $\epsilon = 0.4$ at a strain rate of $\dot{\epsilon} = 10 \text{ s}^{-1}$): (a) microtexture maps: α -fiber in blue and γ -fiber in red; (b) corresponding $\phi_2 = 45^\circ$ section through the orientation distribution function.

occurs by merging LAGBs during subgrain coalescence [35] and subgrain growth by the migration of LAGBs via dislocation motion. From the results presented in this study it is, however, it is not possible to clearly differentiate which of these mechanisms is most relevant for the strong grain refinement observed.

During the large strain warm deformation a further increase in strain above the effective value is beneficial for the formation of HAGBs and for the adjustment of the grain shape. It can be concluded that the process of gradual deformation-induced crystallite subdivision is the essential process for the formation of an ultrafine grained microstructure. In particular pronounced recovery (continuous recrystallization) is a prerequisite to form HAGBs.

4.2. Microstructure evolution of the ferrite during annealing

After 2 h annealing at 823 K, numerous dislocations can still be identified inside the grains, Fig. 9(d). Compared with the microstructure after the large strain deformation there is a minor change in the fraction of HAGBs during annealing (Figs. 4(b) and 5(d)). These

phenomena suggest that a pronounced recovery or respectively extended recovery [36] occurs during the annealing.

As shown in Fig. 4(a) the ferrite grain size hardly changes, but the grain shape becomes more equiaxed during the final heat treatment (the grain shape aspect ratio drops to about 1.6 during annealing). This effect can be attributed to the accumulation of dislocations into subgrain boundaries along the RD and/or subgrain growth in ND.

The kinetics of subgrain growth can be discussed in terms of Fig. 10(a). The occurring curvatures suggest the possibility for pronounced in-grain subgrain coarsening in the microstructure depicted. As reported earlier [37–39] LAGBs typically have a low but not negligible mobility. It is particularly remarkable that some of the occurring misorientations determined in that ferrite subgrain structure (Fig. 10(a)) are of a high-angle character (i.e. $\theta = 20.7$ – 47.8). Two possibilities are conceivable to understand such mixed high- and low-angle grain boundary structures in-grain ferrite microstructures. First, the formation of the HAGBs observed for instance in subgrain “1” could be attributed to the inherited former pro-eutectoid ferrite grain boundaries. An

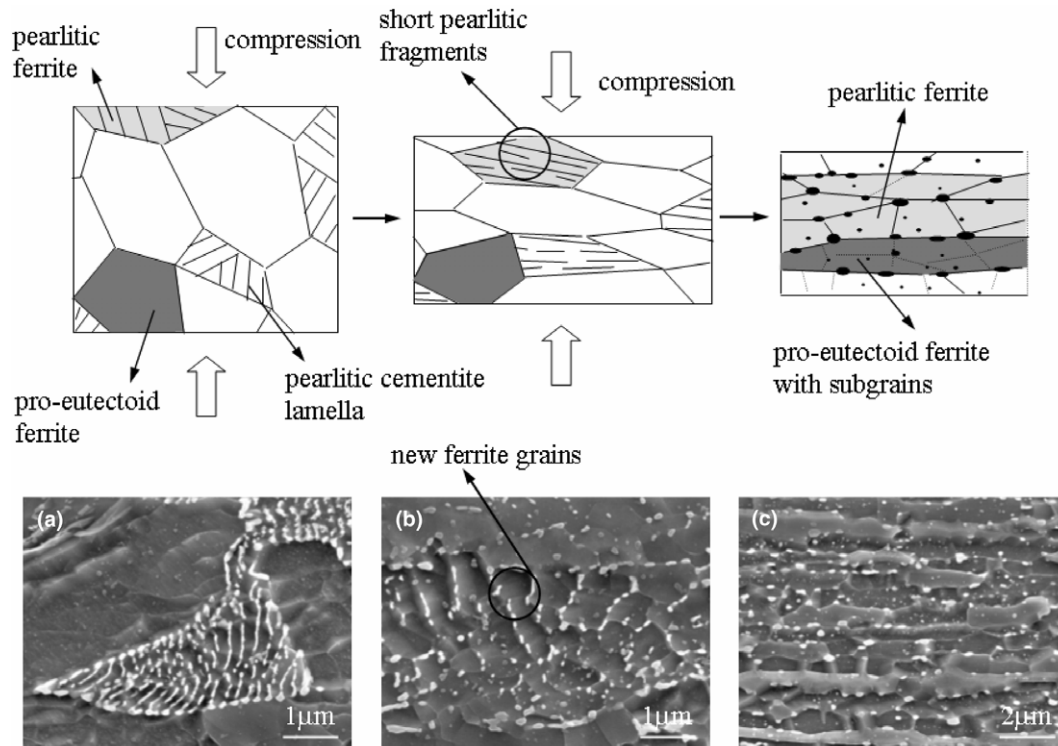


Fig. 8. Upper row: Schematic sketch of the microstructure evolution during warm deformation. Lower row: corresponding SEM micrographs.

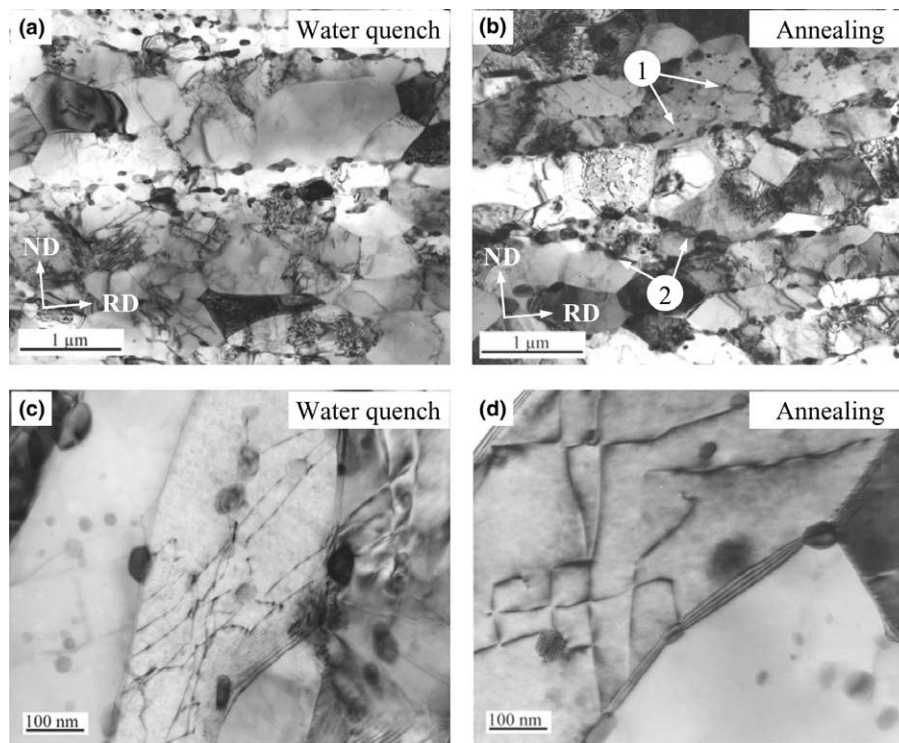


Fig. 9. TEM micrographs of the steel after large strain warm deformation ($\epsilon = 1.6$) and a subsequent 2 h annealing process at 823 K (Fig. 1(b) and (c)): (a,c) deformed microstructure; (b,d) annealed microstructure. (Arrows “1” point at the fine cementite particles inside the ferrite grains. Arrows “2” point at the coarse cementite particles at the ferrite grain boundaries.)

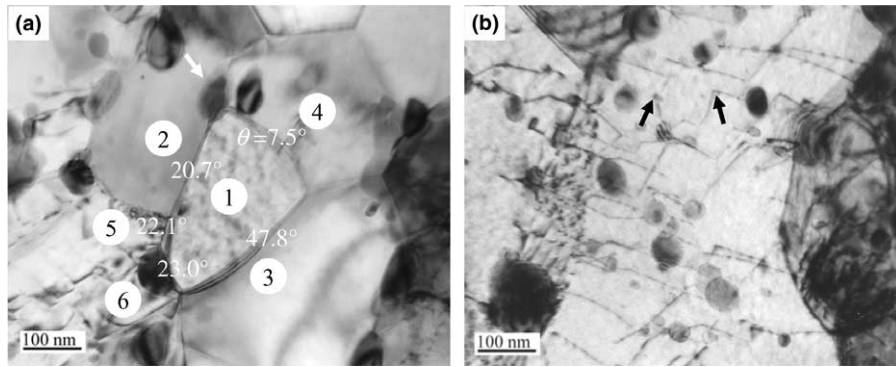


Fig. 10. TEM micrographs of the steel after large strain warm deformation ($\epsilon = 1.6$) and a subsequent 2 h annealing treatment at 823 K (Fig. 1(b)). (a) Mutual crystallographic misorientation of the local areas (adjacent grains and subgrains numbered with 1–6). The white arrow points to a cementite particle pinning the subgrain boundary (misorientation $\theta = 7.5^\circ$). (b) Dislocation structures and individual cementite particles inside the ferrite matrix. The black arrows point at the cementite particles as they pin dislocations.

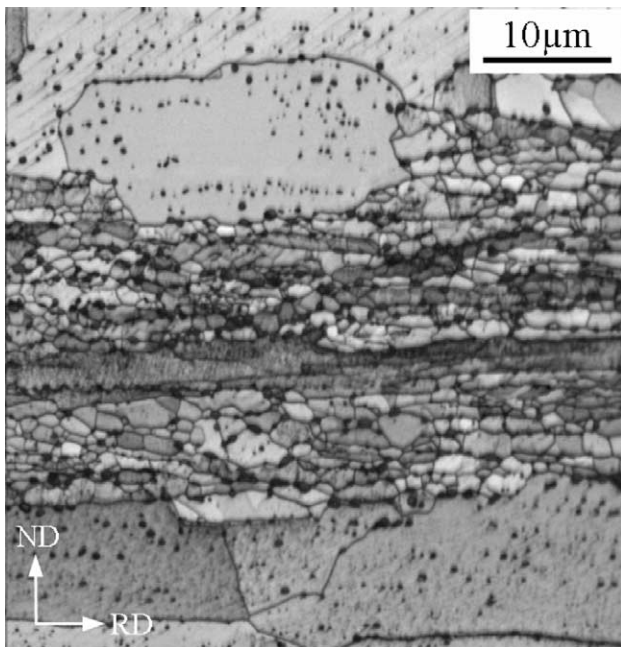


Fig. 11. EBSD image quality map of the steel after large strain deformation ($\epsilon = 1.6$) at 823 K and subsequent 2 h annealing treatment at 973 K (see schematics in Fig. 1(d)).

alternative picture could be that both, the high- and the LAGBs formed due to deformation and continuous recrystallization. The reasons why a *continuous* recrystallization process prevails over a *discontinuous* one during the processes will be discussed in Section 4.5.3.

4.3. Spheroidization of lamellar pearlite

As reported by Robbins and Shepard [40], the driving force for spheroidization in eutectoid steels is the resulting reduction in interfacial area between the cementite lamellae and the ferrite matrix. The carbon content of the ferrite matrix in equilibrium with cementite will,

hence, be much higher at the fragmented ends of the cementite lamellae, where the curvature of the interface is very large, than in areas of small curvature. Therefore, the spheroidization of the cementite lamellae is attributed to carbon diffusion through the ferrite matrix from regions of small radius of curvature to regions of large radius of curvature [41].

The overall process of spheroidization during plastic deformation involves the break-up of lamellae into fragments and the subsequent shape change and competitive Ostwald coarsening of these fragments. Fragments of the former cementite lamellae located at a prior austenite grain boundary can more easily undergo ripening due to an accelerated diffusion along the grain boundary, which leads to an overall faster coarsening of these cementite fragments (see arrow “1” in Fig. 4(c)). According to Chattopadhyay and Sellars [42], all stages of spheroidization during warm deformation are controlled by an effective diffusion coefficient for carbon, which they interpret in terms of a concurrent diffusion mechanism of carbon-vacancy complexes. In contrast, according to the work of Sherby and Harrigan [43,44], strain enhanced spheroidization may also be interpreted in terms of the rate at which iron atoms diffuse away from the cementite- α ferrite interface in order to relieve the compression lattice distortions arising from the formation of new cementite (Fe_3C). Sherby and Harrigan [43,44] came to this conclusion because the activation energy they observed for spheroidization was similar to that for iron diffusion along grain boundaries. An interesting detail in this context is that spheroidization of lamellar pearlite may occur particularly quickly at triple-points owing to the large contact area of the cementite lamellae to grain boundary segments [45].

The rate of cementite spheroidization can be enhanced by six orders of magnitude through warm deformation as compared to a stand-alone annealing treatment [42]. Warm deformation adds excess lattice vacancies to a concentration much above the thermal

equilibrium value. This may happen, for instance, by the motion of jogged screw dislocations. These excess vacancies accelerate diffusion and, therefore, enhance the rate of spheroidization [40].

The appearance of such a former pearlitic cementite lamellae structure is emphasized by arrow “3” in Fig. 3(c) after a large accumulated strain of 1.6. This observation indicates that the spheroidization is not fully finished after the large strain warm deformation. The distribution of small spheroidized cementite particles in the initial pearlite colony (arrow “2” in Fig. 3(c)) as well as the alignments of the cementite particles which decorate the ferrite grain boundaries (arrow “1”) indicate that the mere large strain warm deformation process *without* a subsequent annealing is insufficient for a homogeneous distribution of cementite particles.

4.4. Distribution of cementite particles

Apart from the processes of spheroidization and coarsening of the cementite, which are typical mechanisms occurring in eutectoid steels [46], the process of a homogeneous distribution of cementite after the spheroidization can be observed in the present ferrite-pearlite steel after annealing, Fig. 3(d). This means that after the large strain warm deformation and subsequent annealing treatment cementite particles can also be found even within the former pro-eutectoid ferrite regions. The redistribution of cementite particles during annealing can be interpreted in terms of a dissolution and re-precipitation mechanism [47–50].

In the immediate vicinity of the cementite particles a large number of dislocations are stored during large strain warm deformation. The bonding energy between carbon atoms and edge dislocations in the ferrite is larger than that between the carbon and the iron atoms in the cementite [50]. As a result, the cementite particles dissolve and the carbon atoms in solid solution may diffuse very rapidly via dislocation cores (pipe diffusion) from the areas of the former pearlite colonies to the cementite free areas inside the former pro-eutectoid ferrite. This leads to a supersaturated ferrite matrix with high carbon concentration. This corresponds well with the work of Korznikov et al. [51] where a complete dissolution of cementite particles was observed in a 1.2%C steel processed by large strain deformation.

As discussed in Section 4.2 the annealing treatment goes along with pronounced recovery. This leads to a decrease in the dislocation density by annihilation processes. Therefore, the solubility of carbon atoms in the ferrite matrix drops with the decrease in the dislocation density, which results in the precipitation of cementite inside the ferrite matrix. As a result the cementite particles are distributed rather homogeneously in the ferritic matrix (Fig. 3(d)). It is, hence, not possible any longer to

distinguish between the initial pearlite and the pro-eutectoid ferrite regions, as shown in Fig. 8(a).

An important condition for the redistribution of cementite, as suggested in [52], seems to be a high dislocation density in terms of pipe diffusion in the heavily deformed initial pearlite colonies, which was estimated to be of the order of 10^{16} m^{-2} for a low carbon steel. In case of a plain low carbon steel [52] with low recrystallization temperature, recrystallization would slow down or even stop the re-distribution of cementite by significantly reducing the dislocation density. As a result, some pearlite colonies may still exist even after annealing [52]. However, a microalloyed low carbon steel with higher recrystallization temperature offers the possibility that only recovery takes place even at fairly high temperatures. In this situation the dislocation density will not be reduced significantly, so that the redistribution of cementite can take place assisted by fast pipe diffusion along the dislocation cores.

4.5. Effect of cementite particles

4.5.1. Ferrite grain size

A fine cementite particle dispersion inside the ferrite matrix may exert a strong pinning effect on individual dislocations at certain temperatures. Geometrically necessary dislocations will generate an inhomogeneous dislocation structure around these particles. This facilitates the formation of new subgrain boundaries inside a ferrite grain. New HAGBs can form preferably by such particle-stabilized subgrain boundaries [36] so that this mechanism might promote the formation of refined continuously recrystallized ferrite grains. On the other hand, the presence of these fine cementite particles drastically retards the softening of the ferrite in the areas of the former pearlite colonies (arrow “2” in Fig. 3(c)). The formation and growth of the ferrite subgrains are controlled by solute carbon and by the fine cementite particles. Consequently, the spacing of the particles determines the size of the subgrains [30,41].

4.5.2. High temperature (823 K) stability of ferrite against grain coarsening

Once an ultrafine microstructure is formed, an average grain size of $1.3 \mu\text{m}$ was found to be stable in the steel after 2 h annealing at 823 K (Fig. 4(a)). This enormous topological stability can be attributed to the homogeneously distributed fine cementite particles which are themselves fairly stable against coarsening even after annealing in this temperature regime. The fine particles impede grain boundary motion owing to Zener pinning.

4.5.3. Inhibition of primary recrystallization

As shown in Fig. 9(c), (d) and Fig. 10(b), a large number of dislocations exists in both the deformed

and also in the annealed specimens. This demonstrates that recrystallization does not prevail during the deformation/annealing processing described above. The reason that mainly *continuous* rather than *discontinuous* recrystallization takes place may be interpreted as follows: Due to the spheroidization of the pearlitic cementite lamellae during warm deformation, fine cementite particles are observed in the microstructure after the imposed large strain deformation. The fine particles lead to a high dragging force for the migration of grain boundaries due to Zener pinning. On the other hand, it is known that due to the high stacking fault energy dislocation recovery in the ferrite can proceed very fast. This means that the dislocation-rearrangement, which is a prerequisite to form energetically more favorable grain boundary configurations, is easily initiated everywhere in the material, but the subsequent migration of the newly formed (high-angle) grain boundaries are quickly pinned owing to the presence of the fine carbides.

4.6. Evolution of the crystallographic texture during annealing

After large strain deformation the texture of the samples consists of the α - and γ -fibers which are typical of rolled ferritic steels [17–23,53–55]. However, after annealing these samples, the strong α -fiber observed after deformation not only prevails but is even enhanced (Figs. 6 and 7). The microstructure of the annealed material still consists of elongated ferrite grains (Figs. 3(d) and 4(a)) with a relatively high dislocation content (Figs. 9(d) and 10(b)) which indicates that no substantial recrystallization has occurred. The texture and microstructure observations may be explained as follows: (i) The occurrence of recrystallization is impeded by cementite particles which may inhibit either the nucleation or the growth stage of newly recrystallized grains. (ii) Due to the higher stored energy of γ -fiber-oriented grains as compared to α -fiber-oriented grains the latter slowly consume their γ -fiber neighbors, thereby, preserving their internal α -fiber subgrain structure. This means that both, the texture and the microstructure observed strongly support the suggested process of pronounced recovery.

5. Conclusions

A plain C–Mn steel with ultrafine ferrite grains (average grain size of 1.3 μm) and homogeneously distributed cementite particles was produced by large strain warm deformation ($\varepsilon = 1.6$) and subsequent annealing. The ultrafine microstructures were stable against grain and particle coarsening even during a 2 h annealing treatment at 823 K. We observed a critical strain of ~ 0.8 which was required as a lower bound for efficiently refin-

ing the microstructure. A further increase in strain over this value is beneficial for the formation of a higher fraction of HAGBs and the adjustment of the ferrite grain towards more spherical shapes. The basic results and conclusions are given in the following:

- (1) The grain refinement by large strain warm deformation was explained in terms of a continuous recrystallization process. Deformation induced grain subdivision is essential for the formation of ultrafine grained microstructures. Pronounced recovery processes are necessary to form HAGBs.
- (2) During a 2 h heat treatment at 823 K after the large strain deformation procedure grain growth was suppressed. Pronounced recovery at this stage together with the presence of fine carbides suppressing discontinuous recrystallization facilitated the formation of HAGBs and the evolution of a more equiaxed grain shape.
- (3) Spheroidization of pearlitic cementite lamellae during the large strain warm deformation was assumed to be accelerated by fragmentation of cementite lamellae and by the assistance of pipe diffusion. During the deformation-annealing cycle, the fine cementite particles may dissolve and some of that carbon in solid solution can then diffuse from the areas of the former pearlite colonies to the cementite free areas inside the former pro-eutectoid ferrite followed by subsequent re-precipitation and competitive coarsening.
- (4) Fine cementite particles are beneficial for the formation of a fine ferritic grain structure. They inhibit efficiently grain boundary migration due to Zener pinning. This effect stabilizes the ultrafine grains against grain coarsening. It is also assumed to inhibit primary recrystallization. The presence of such fine cementite particles results in an increase of the effective recrystallization temperature which widens the temperature windows for corresponding advanced rolling and annealing treatments.
- (5) The strong α -fiber textures observed which are typical of rolled but not of recrystallized steels are in excellent agreement with the suggested pronounced recovery process. The absence of the motion of newly formed HAGBs explains the absence of a texture transition from the α -fiber to the γ -fiber texture.

Acknowledgement

The authors express their gratitude for the financial support of the European Coal and Steel Community (ECSC). Project title: ultrafine grained steel by innovative deformation cycles; number: 7210-PR/288.

References

- [1] Valiev RZ. *Mater Sci Eng A* 1997;234:59.
- [2] Segal VM. *Mater Sci Eng A* 1999;271:322.
- [3] Saito Y, Utsunomiya H, Tsuji N, Sakai T. *Acta Mater* 1999;47:579.
- [4] Tsuji N, Ueki R, Minamino Y. *Scripta Mater* 2002;47:69.
- [5] Inoue T, Torizuka S, Nagai K. International symposium on ultrafine grained steels (ISUGS 2001). Fukuoka, Japan: The Iron and Steel Institute of Japan; 2001. p. 88–91.
- [6] Hodgson PD, Hickson MR, Gibbs RK. *Scripta Mater* 1999;40:1179.
- [7] Kaspar R, Distl JS, Pawelski O. *Steel Res* 1988;59:421.
- [8] Matsumura Y, Yada H. *ISIJ Int* 1987;27:492.
- [9] Najafi-Zadeh A, Jonas JJ, Yue S. *Metall Trans A* 1992;23:2607.
- [10] Shin DH, Kim BC, Kim YS, Park KT. *Acta Mater* 2000;48:2247.
- [11] Tsuji N, Saito Y, Utsunomiya H, Tanigawa S. *Scripta Mater* 1999;40:795.
- [12] Belyakov A, Tszuzaki K, Miura H, Sakai T. *Acta Mater* 2003;51:847.
- [13] Nanba S, Nomura M, Matsukura N, Makii K, Shirota Y. International symposium on ultrafine grained steels (ISUGS 2001). Fukuoka, Japan: The Iron and Steel Institute of Japan; 2001. pp. 286–89.
- [14] Jansson B, Schalin M, Sundman B. *Phase Equilibria* 1993;14:557.
- [15] Kaspar R, Pawelski O. *Materialprüfung* 1989;31:14.
- [16] Song R, Ponge D, Kaspar R, Raabe D. *Zeitschrift für Metallkunde* 2004;95:513.
- [17] Hölscher M, Raabe D, Lücke K. *Steel Res* 1991;62:567.
- [18] Raabe D, Lücke K. *Scripta Metall Mater* 1992;27:1533.
- [19] Raabe D. *Steel Res* 1995;66:222.
- [20] Huh MY, Raabe D, Engler O. *Steel Res* 1995;66:353.
- [21] Hutchinson WB. *Int Mater Rev* 1984;29:25.
- [22] Ushioda K, Hutchinson WB, Agren J, Schlippenbach UV. *Mater Sci Technol* 1986;2:807.
- [23] Raabe D, Lücke K. *Mater Sci Forum* 1994;157–162:597.
- [24] Hutchinson W. *Acta Mater* 1989;37:1047.
- [25] Raabe D. *Steel Res* 2003;74:327.
- [26] Raabe D, Zhao Z, Park SJ, Roters F. *Acta Mater* 2002;50:421.
- [27] Zaefferer S. *Adv Imaging Electron Phys* 2002;125:355.
- [28] Zaefferer S. *J Appl Cryst* 2000;33:10.
- [29] Apps PJ, Bowen JR, Prangnell PB. *Acta Mater* 2003;51:2811.
- [30] Gholinia A, Humphreys FJ, Prangnell PB. *Acta Mater* 2002;50:4461.
- [31] Tsuji N, Toyoda T, Minamino Y, Koizumi Y, Yamane T, Komatsu M, et al. *Mater Sci Eng A* 2003;350:108.
- [32] Haessner F. *Recrystallization of metallic materials*, Dr. Riederer Verlag, 1984.
- [33] Doherty RD, Hughes DA, Humphreys FJ, Jonas JJ, Jensen DJ, Kassner ME, et al. *Mater Sci Eng A* 1997;238:219.
- [34] Hales SJ, Mcnelley TR, Mcqueen HJ. *Metall Trans A* 1991;22:1037.
- [35] Hornbogen E. *Metall Trans A* 1979;10:947.
- [36] Humphreys FJ, Hatherly M. *Recrystallization and related annealing phenomena*. UK: Pergamon; 1995. p. 167, 164.
- [37] Doherty RD. *Nucleation*. In: Haessner F, editor. *Recrystallization of metallic materials*. Dr. Riederer Verlag GmbH; 1978. p. 42.
- [38] Winning M, Gottstein G, Shvindlerman LS. *Acta Mater* 2001;49:211.
- [39] Winning M, Gottstein G, Shvindlerman LS. *Acta Mater* 2002;50:353.
- [40] Robbins JK, Shepard OC, Sherby OD. *Iron Steel Inst* 1964;202:804.
- [41] Storoyeva L, Ponge D, Kaspar R, Raabe D. *Acta Mater* 2004;52:2209.
- [42] Chattopadhyay S, Sellars CM. *Acta Metall* 1982;30:157.
- [43] Sherby OD, Harrigan MJ, Chamagne L, Sauve C. *Trans ASM* 1969;62:575.
- [44] Harrigan MJ, Sherby OD. *Mater Sci Eng* 1971;7:177.
- [45] Ho E, Weatherly GC. *The Metal Soc* 1977;4:141.
- [46] Kaspar R, Kapellner W, Lang C. *Steel Res* 1988;59:492.
- [47] Languillaume J, Kapelski G, Baudelet B. *Acta Mater* 1997;45:1201.
- [48] Ivanisenko Y, Lojkowski W, Valiev RZ, Fecht HJ. *Acta Mater* 2003;51:5555.
- [49] Badmos AY, Bhadeshia H. *Metall Mater Trans A* 1997;28A:2189.
- [50] Gavriljuk VG. *Scripta Mater* 2001;45:1469.
- [51] Korznikov AV, Ivanisenko YV, Laptionok DV, Safarov IM, Pilyugin VP, Valiev RZ. *Nanostruct Mater* 1994;4:159.
- [52] Shin DH, Park KT, Kim YS. *Scripta Mater* 2003;48:469.
- [53] Hölscher M, Raabe D, Lücke K. *Acta Metall Mater* 1994;42:879.
- [54] Raabe D. *Mater Sci Eng A* 1995;197:31.
- [55] Raabe D, Lücke K. *Mater Sci Technol* 1993;9:302.